Engineering Structures 226 (2021) 111306

Contents lists available at ScienceDirect

Engineering Structures

journal homepage: www.elsevier.com/locate/engstruct

Cyclic behavior of c-shaped composite plate shear walls – Concrete filled

Hadi Kenarangi [a], Emre Kizilarslan [b,*], Michel Bruneau [b]

[a] Modjeski and Masters, Inc., 100 Sterling Pkwy #302, Mechanicsburg, PA 17050, United States
[b] Dept. of Civil Structural and Environmental Engineering, Univ. at Buffalo, Buffalo, NY 14260, United States

ARTICLE INFO

Keywords:
Composite plate shear walls
Cyclic testing
Inelastic behavior
Flexural behavior
Ductility
Plate buckling
Fracture
Strength degradation

ABSTRACT

A Composite Plate Shear Wall/Concrete Filled (C-PSW/CF) is a special lateral-force resisting system consisting a sandwiched panel of two steel plates with concrete infill in between them, ideally suited for core-wall structures in high-rise construction. The steel plates are connected to each other using tie bars that are embedded in the concrete infill and, in some instances, steel-headed stud anchors. This research project was conducted to investigate the cyclic lateral load behavior of these walls, in terms of strength, and drift capacity. The testing program includes two large-scale C-shaped concrete filled composite plate shear core walls subjected to flexure and axial loads together. Their dimensions were the same, but different axial loads were applied up to 19% of axial loading capacity. The composite behavior and the plastic hinge development were investigated and compared to results from plastic moment calculations. This provides valuable results on the expected behavior of one composite cross-section that is frequently used in full core wall. This is done to support the development of design guidelines for high-rise core-wall steel buildings having C-PSW/CF as the primary lateral force resisting system.

1. Introduction and background

A Composite Plate Shear Wall/Concrete Filled (C-PSW/CF) is a special lateral-force resisting system consisting of a sandwiched panel of two steel plates with concrete infill in between them. The steel plates are connected to each other using tie bars that are embedded in the concrete infill as in Fig. 1 and, in some instances, steel-headed stud anchors. C-PSW/CF is lateral load resisting systems ideally suited for core-wall structures in high-rise construction (as well as other shear wall applications).

In tall building construction, reinforced concrete shear walls with coupling beams are commonly used. The C-PSW/CF can similarly be used with composite coupling beams. Their appeal lies in the fact that the steel panels of C-PSW/CF can be fabricated off-site, shipped and erected on-site, and serve as formwork for the concrete. This can significantly accelerate construction time [1]. While this structural system has been used in mid-rise construction in non-seismic regions [2], as well as nuclear structures to provide (among many load cases considered) missile and aircraft impact resistance in addition to elastic resistance to seismic and wind lateral loads [3–5], knowledge on its cyclic inelastic non-linear behavior is needed for application in regions where severe earthquakes are expected. In a somewhat related topic, past research that has shown that concrete-filled steel tubes can have a ductile cyclic inelastic behavior [6–15] is instructive and suggests that similar performance is possible for C-SPW/CF, although this cannot be inferred directly from those past tests.

Some research has investigated in-plane cyclic inelastic behavior. Alzeni and Bruneau [16] tested four concrete-filled sandwich steel panel (CFSSP) walls with and without circular boundary elements. The specimens showed stable ductility up to 3% drift. A few wall specimens having square ends rather than circular ones have also been tested [17–20]. However, no research has been conducted on C-Shaped walls, especially when subjected to simultaneously axial and lateral loadings. Given that C-shaped walls can be parts of the lateral-load resisting core of building (around elevator shafts), investigating the behavior of such walls is important. Note that in these walls, the plastic neutral axis can move quite significantly in alternating directions of loading. This knowledge is necessary for the subsequent further development of design guidelines when high-rise core-wall steel buildings having C-PSW/CF are used as the primary lateral force resisting system.

With the above in mind, two C-PSW/CFs were tested at the Structural Engineering and Earthquake Simulation Laboratory (SEESL) at State University of New York (SUNY) at Buffalo. The dimensions of the walls were the same, but slightly different axial load ratios were applied,

* Corresponding author.
E-mail addresses: hadikena@buffalo.edu (H. Kenarangi), emrekizi@buffalo.edu (E. Kizilarslan), bruneau@buffalo.edu (M. Bruneau).

https://doi.org/10.1016/j.engstruct.2020.111306
Received 9 February 2020; Received in revised form 21 July 2020; Accepted 7 September 2020
Available online 10 October 2020

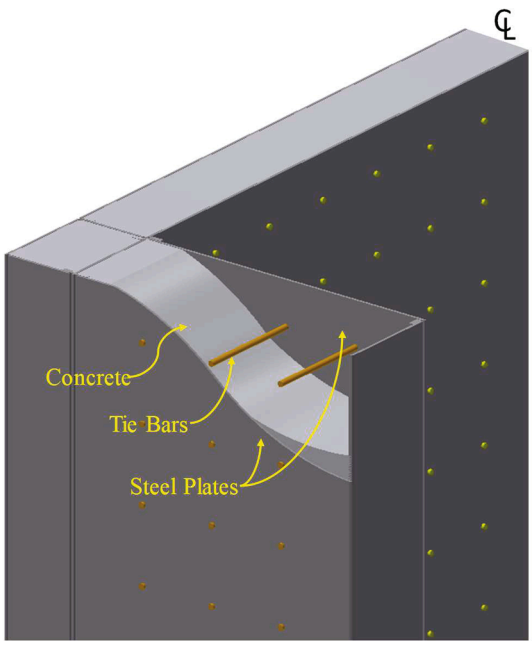

Fig. 1. The main components of C-PSW/CF.

namely corresponding to 19% and 15% of the crushing load of the infill concrete ($A_c f'_c$). Testing two specimens was helpful to establish replicability of the test results. The findings from this experimental program are presented here. Note that the cyclic response and progressive failure modes of the specimen are presented in significant details to dissipate some common misconceptions and misinterpretations related to the cyclic inelastic behavior of composite walls.

2. Test specimens and setup

A series of two cyclic large-scale tests were conducted on cantilever composite walls having C–Shaped cross-section in plan. To be able to test representative C-shaped walls in the laboratory, the cross-section dimensions of the prototype model needed to be scaled down. The available minimum thickness of 3/16in. for hot-rolled steel plates dictated the geometric scale factor of the specimens, corresponding to a scale factor of 3/8 for cross-section dimensions. This scaling also made it possible to apply significant axial load on the specimen (planned to be up to 22% as will be described later). The specimens were designed to have aspect ratios of cross-section ($\gamma = b/h$), web ($\beta = c/b$), and flange ($\alpha = d/h$) within ± 35% of those from the prototype model (i.e., defined by the practicing engineers on the Project Advisory Team to be $\gamma_p = 0.33$, $\beta_p = 0.21$, and $\alpha_p = 0.07$**).** Fig. 2a shows the definition of these cross-sectional aspect ratios.

Fig. 2b shows approximately 15,000 possible cross-sections that were considered during the specimen design process. The rectangular box shown in this figure indicates the boundaries of the above imposed constraints on cross-sectional aspect ratios. Note that the final design was chosen from the points located inside the box shown in Fig. 2b, but also taking into account a number of experimental constraints – for example, the specimen cross-section could not block the DYWIDAG bar locations shown in Fig. 2c. These experimental constraints further limited the possible choice of specimens down to only a few (nearly similar) options. Fig. 2c shows the cross-section of the selected final design and its position on the footing. The dimensions and properties of selected specimens are: wall height, H = 166in. (4216 mm); flange length, h = 97.5in. (2476.5 mm); web length, b = 30in. (762 mm); steel plate thickness, t = 0.1875in. (4.76 mm); flange thickness, d = 6in. (152.4 mm); web thickness, c = 8.375in. (212.73 mm); tie spacing = 6in. (152.4 mm); tie diameter = 0.5in. (12.7 mm); wall aspect ratio, H/b = 5.53; cross-section aspect ratio, $\gamma = b/h = 0.31$; flange aspect ratio, $\alpha = d/h = 0.06$; web aspect ratio, $\beta = c/b = 0.28$; steel area, A_s = 61.8in^2 (39871 mm^2); concrete area, A_c = 9225.2in^2 (5951730 mm^2); reinforcement ratio of web, ρ_{web} = 4.5%; reinforcement ratio of flange, ρ_{flange} = 6.3%, and; reinforcement ratio, ρ_s = 6.3%. The length of the tie bars in the flanges was 6.375in. (162 mm), and in the webs 8.75in. (222.25 mm) (and 0.375 in. (9.53 mm) longer inside the footing to accommodate the thicker plate used there). For more information on the strength and behavior comparisons between the selected specimens and the prototype model, refer to [20]. For the detailing at wall flange corners, two steel plates in the web were bent 90 degrees, in an L-shape, and connected with full penetration (CJP) welds using backup bar along height at the cross-section corners. For the corner box section, again one plate was bent 90 degrees and the box was closed using a straight plate. For the flanges, two straight plates were used and welded to corner plates with CJP welds. The details of the welds and where plates were bent are shown in Fig. 2d.

For each one of the specimens, the formwork for the concrete footing was first constructed. PVC pipes were placed inside the footing on a 2ft. center-to-center grid at the locations where DYWIDAG bars [21] were to be used to connect the specimens to the SEESL strong floor. The reinforcing cage of the footing was tied outside the formwork and then placed in the formwork. Then the empty steel plate module of the wall was positioned into the formwork, clearing the reinforcing bar cages. Additional #10 bars were then run through the wall's flange part that is embedded in the footing (in pre-drilled holes) to achieve continuity of the horizontal reinforcement in the cage. The pre-drilled holes on the flange through which the #10 bars passed were sealed to prevent the flow of wet concrete between the wall and the footing. One week after the footing concrete was poured, the footing formwork was removed and the specimen was positioned at its testing location in front of the SEESL strong wall. The specimen was then post-tensioned to the strong floor using 24 DYWIDAG bars with 1–3/8in. (34.93 mm) nominal diameter. The DYWIDAGs were post-tension with 130kips force, which was equal to 70% of their nominal yield load. Next, concrete was cast into the walls, and 54 strain gauges, displacement transducers (28 string potentiometers and 6 linear potentiometers), and other instrumentation were installed. The loading set-up consisted of two vertically inclined actuators (oriented at about 70 degrees from the horizontal) used to apply an axial load to the specimen, and two lateral actuators to apply cyclic lateral loading. Fig. 3 shows some of the above steps of the test setup preparation. The detail of the footing is illustrated in Fig. 4. In this detail, a base plate prevents uplifting of the wall by engaging the adjacent concrete and stiffeners are used to avoid bending of the base plate. Thicker wall plates are used inside of the footing to prevent yielding and fracture of the plates inside of the footing (particularly due to holes in the plate that accommodate the #10 reinforcing bars running through the wall). Similar details have been used for composite walls by Alzeni and Bruneau [16], and for composite concrete filled columns by Kenarangi and Bruneau [9], and Lehman et al [22].

The design set-up to apply vertical loading to the specimen consisted of a top attachment fixture that is a stiffened inverted T-shape built-up beam sitting on top of the wall's flange. The top fixture spreads the downward load of the actuators on top of the wall. Two inclined vertical actuators were post-tensioned to the strong floor and located symmetrically on the east and west sides of the wall. Horizontal component of the force from the actuators were designed to be transferred to the footing using I-beams inserted between the actuator plate and the footing. The load of each actuator was transferred to the top attachment fixture by means of four high impact threaded bars. Fig. 5 shows a schematic view of this system. Double spherical washers were used at the threaded bar joints in order to avoid moment concentrations due to accidental eccentricities. Fig. 6 shows the details of the threaded bar end joints. More details of the foundation, the top fixture, and the actuator attachment plates and their design procedures can be found in Bruneau et al. [23].

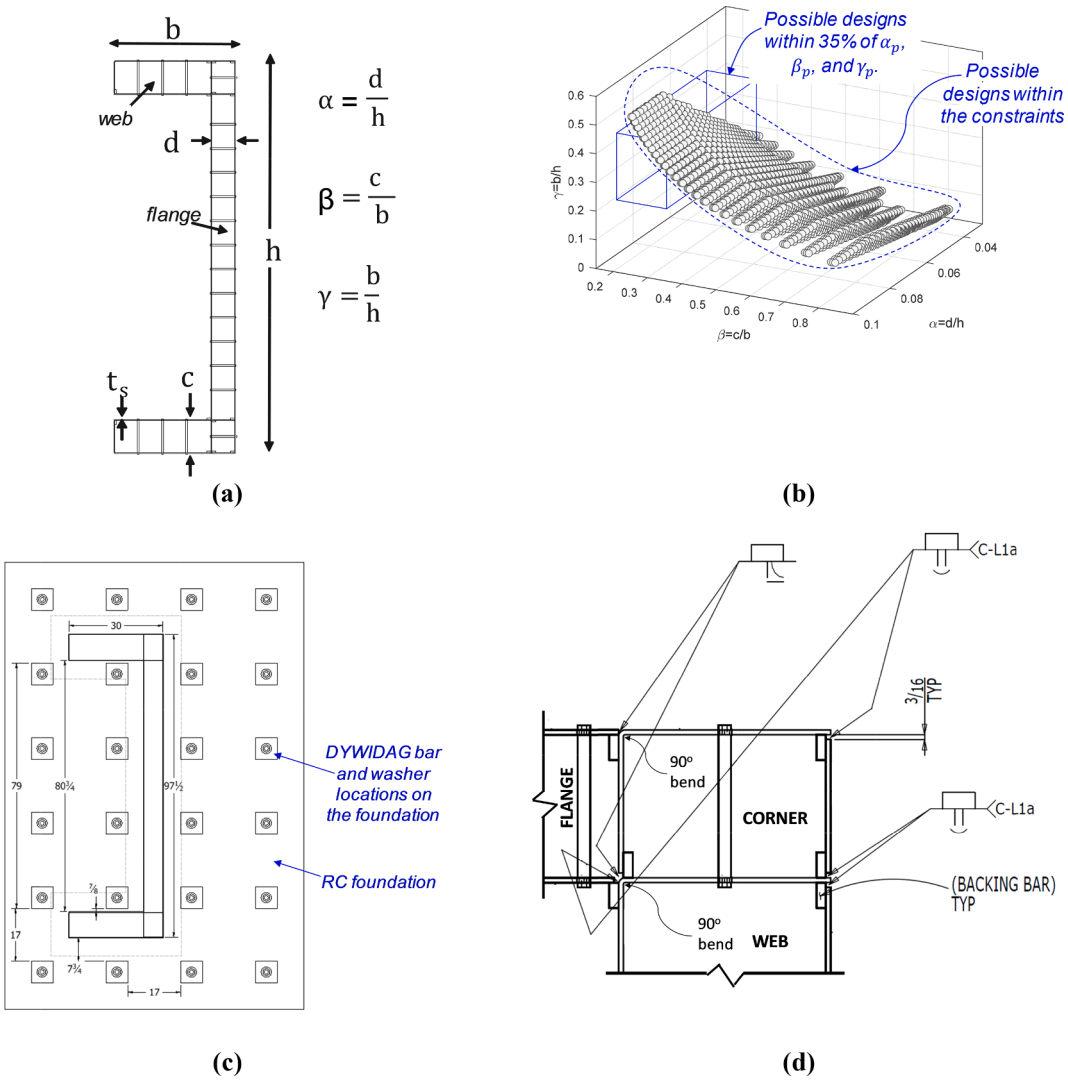

Fig. 2. (a) Representation of C-Shaped wall section and aspect ratios, (b) design space of the 15,000 possible cross-sections considered, (c) position of the wall on the footing plan, and; (d) connection details of the corner.

Fig. 3. Construction sequence of specimens and test setup.

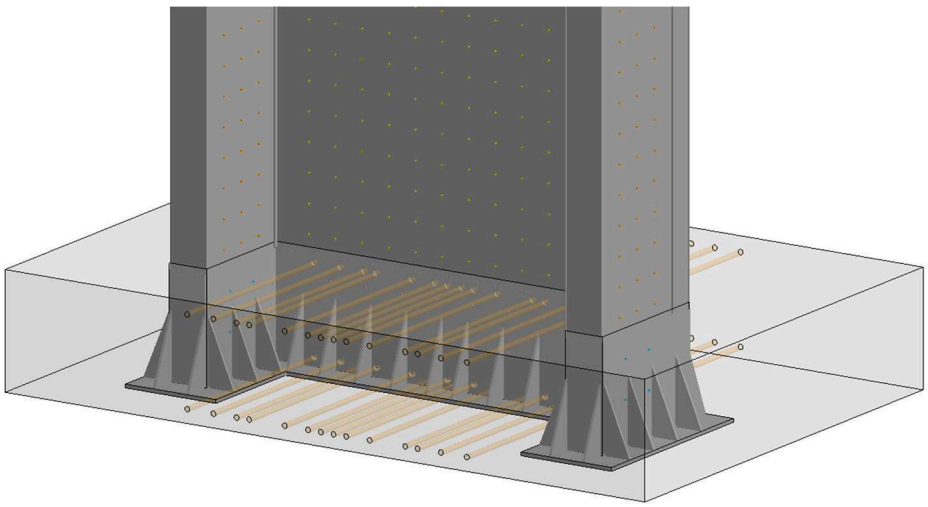

Fig. 4. Composite wall-to-basemat connections with wall embedded into concrete footing.

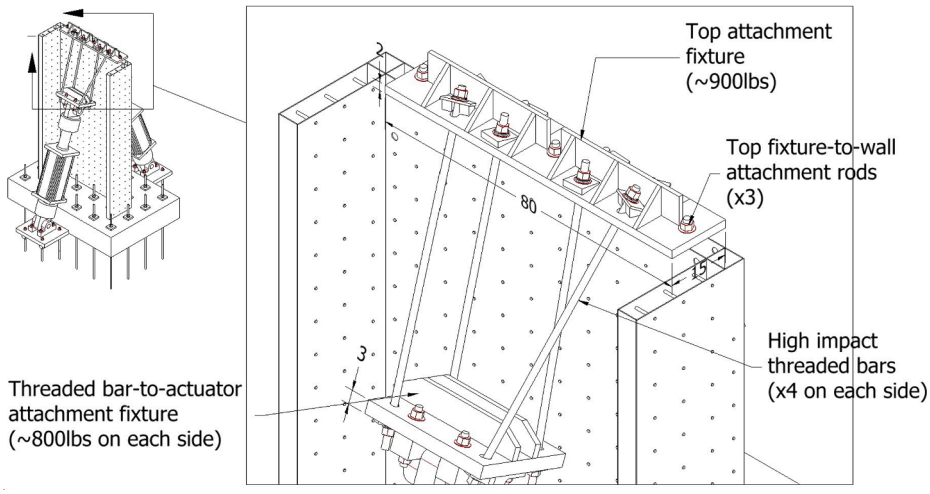

Fig. 5. Schematic view of the vertical loading system.

Fig. 7 represents a three-dimensional (3D) rendering of the test specimen and setup. Note that the subsequent description of the specimens' behavior will refer to cardinal points to locate the development of various limit states. For this purpose, the North direction is shown for the specimens in Fig. 7.

3. Material properties of specimens

Three coupons from the steel used in the webs and flange of the specimen (refer to Fig. 2a) were tested under uniaxial tension, for a total of six coupon tests for each wall specimen. A572 Gr50 steel was used in construction of the flange and web plates. However, no "yield plateau" was observed in the stress–strain behavior of the tested coupons. Using the 0.2% offset method, the yield strengths of the plates were determined to be 54.6ksi (376.5 MPa) and 56.2ksi (387.5 MPa) for web and flange plates of the first specimen (which will be referred as Specimen C1 this point forward), and 52.65ksi (363 MPa) and 57.79ksi (398.4 MPa) for web and flange plates of the second specimen (which will be referred as Specimen C2 this point forward), respectively. The average yield strengths of the plates are 55.4ksi (382 MPa) for Specimen C1 and 55.2ksi (380.6 MPa) for Specimen C2. The tie bars were F1554 Grade 55 steel with specified yield and ultimate strength of 55ksi (379 MPa) and 75ksi (517 MPa), respectively.

For concrete, fifteen 3in. × 6in. (76.2 mm × 152.4 mm) and six 6in. × 12in. (152.4 mm × 304.8 mm) cylinders were taken for each specimen on the days of concrete pouring from the concrete batches used for the footing and the infill of the wall. This unusually large number of cylinders was taken to keep track of concrete strength over time, to ensure that the concrete strength in the first wall would not exceed 4ksi (27.6 MPa) on the day of testing, which was intended to be a target value of $0.22A_c f'_c$ as an axial load when using the vertical actuators at their full capacity (i.e., nominal 450kips (2001.7kN) each). Concrete strength had almost reached 4ksi (27.6 MPa) when tested on a Friday, so testing of Specimen C1 was scheduled at once. However, when testing started on the following Monday, concrete strength had already reached 4.5ksi (31 MPa), enabling attainment of only 19% of the crushing load of concrete ($A_c f'_c$) for this specimen. For Specimen C2, the concrete was allowed to cure for more than 28 days with the intent to reach an expected strength of 6ksi but concrete strength plateaued at 5.1ksi (35.2 MPa) after 30 days and up to 51 days, and testing proceeded by adjusting the axial load in the vertical actuators to apply 15% of the crushing load of concrete ($A_c f'_c$).

4. Loading protocol

Preliminary models were developed based on a previous study by Kenarangi and Bruneau [24] using fully integrated shell elements for steel, beam elements with Hughes-Liu with cross section integration

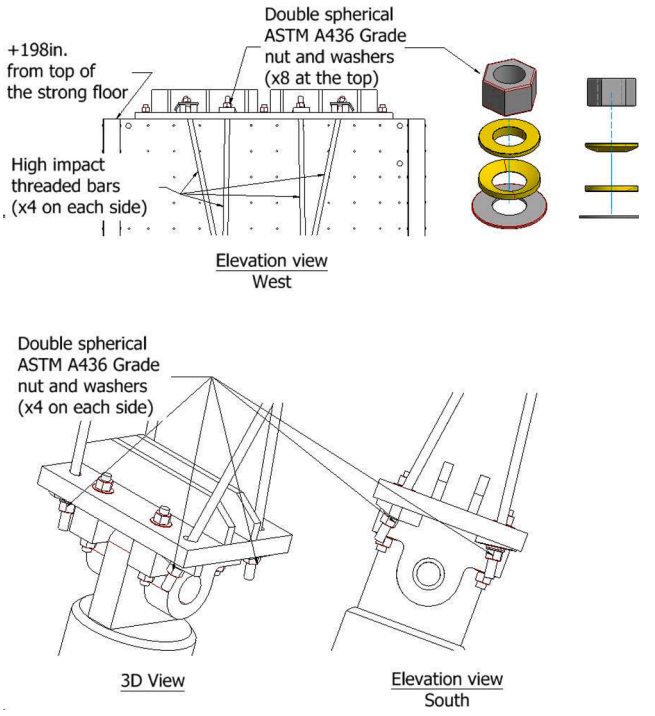

Fig. 6. Threaded bars connection details in the vertical loading system.

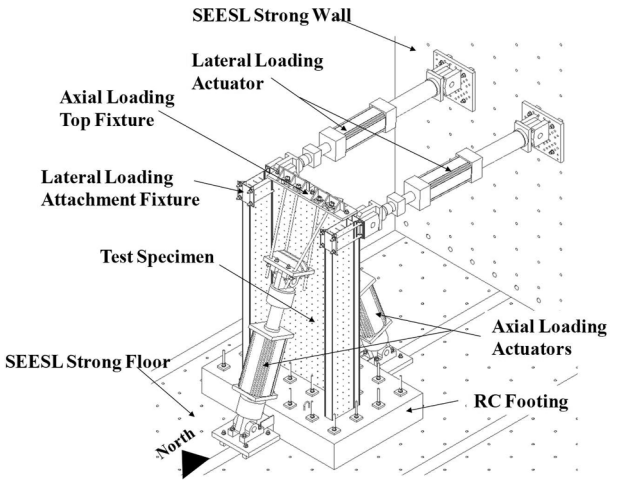

Fig. 7. 3D representation of test setup.

formulation for tie bars, and constant stress solid elements for concrete. Material models used for steel plate, tie bars, and concrete are Piecewise Linear Plasticity, Plastic Kinematic, and Winfrith Concrete models, respectively. The cyclic testing protocol was designed based on the yield displacements obtained from the Finite Element Analysis (FEA) push-over of Specimen C1. The result of the average of steel coupon tests (F_y is 55.4ksi (382 MPa)) was directly input into the model and the concrete strength was assumed to be 4ksi (27.6 MPa). The first yield displacements (Δ_y) in the positive (webs in compression) and negative (flange is in compression) loading directions were obtained at the points where the first yield in the steel plate occurred in the pushover analysis of the LS-DYNA [25] model of the full test setup, which were at $\Delta_y = 1$in. (25.4 mm) and −0.5in. (-12.7 mm), respectively. The pushover curve from the FEA was then bi-linearized and equivalent yield displacements (Δ_y') were calculated as 1.75in. (44.5 mm) and −1.5in. (38.1 mm) in positive and negative directions, respectively. The cyclic loading protocol was designed using the equivalent yield displacements for both directions.

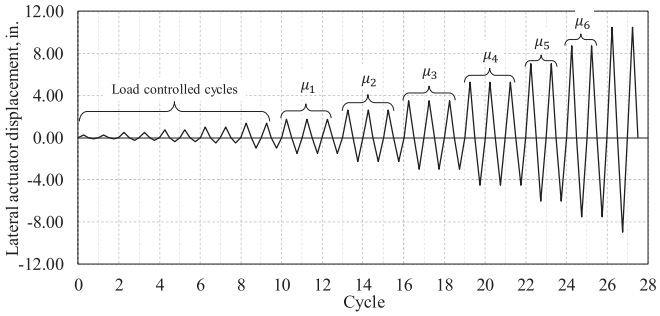

Fig. 8. Loading protocol for C-Shaped specimens.

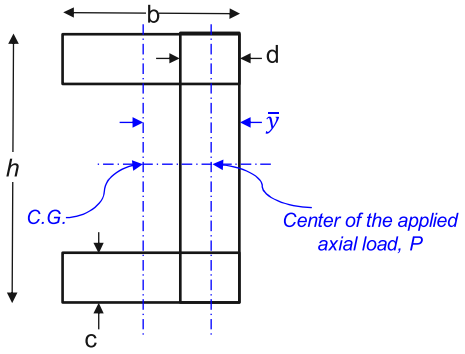

Fig. 9. Location of centroid and centerline of axial load for C-Shaped wall specimens.

To facilitate comparison, both specimens were subjected to the same cyclic displacement loading protocol that was created for Specimen C1.

Up to the equivalent yield displacements ($\mu_1 = \Delta_y$'=+1.75in./-1.5in. (+44.5 mm /-38.1 mm)), the specimens were tested in force-controlled mode (i.e., for the first 10 cycles). Beyond that point, the specimens were tested in displacement-controlled mode for the horizontal actuators (the vertical actuators remained in force-controlled mode throughout the tests). The resulting loading protocol is shown in Fig. 8. Note that there are only two cycles per drift amplitude in the force-controlled cycles. However, the number of cycles per drift amplitude in the displacement-controlled cycles increased to three up to maximum capacity of specimens ($\mu_3 = 3 \times \Delta_y$'= +5.25in./-4.50in. (+133.4 mm /-114.3 mm)), after which the number of cycles decreased to two per displacement amplitudes for the subsequent cycles. Note that the original protocol contains only two cycles at 6% drift, but, as will be shown later, specimens were cycled repeatedly beyond that, as needed to observe the further progression of fracture. Drifts were limited to 6% for safety reasons, to keep the specimen stable upon substantial strength degradation.

5. Application of axial loading on the specimens

The centroid of the specimens is located at$\bar{y}$ = 9.11in. (231.4 mm) from the outside face of the flange. However, for practical reasons in the test set-up design, the axial loading resultant was applied centered on the top of flange rather than at the section centroid. Fig. 9 shows a schematic of the location of the section centroid (i.e., C.G.) and the theoretical center of the applied axial load. This distance between the centroid and center of the axial load resulted in a moment due to the eccentricity of the axial load, which was taken into account when post-processing the experimental results. Moreover, before applying the axial loading, the horizontal actuators were "locked" at their initial point of zero horizontal displacement to prevent the specimens from moving laterally upon application of the axial load due to the moment created by the eccentricity of the axial load.

Table 1
Experiment log of Specimen C1 (Note: 1 in. = 25.4 mm; 1ft = 0.3048 m; 1sq in. = 645.2 mm^2; 1 in^4 = 416231 mm^4; 1 psi = 0.0069 MPa; 1 ksi = 6.9 MPa).

Cycle No	Cycle Drift, in	Laterally Applied Force, V, kips	FE	NWW	NWN	NWS	SWW	SWN	SWS	NWE	SWE
15	2.63/-2.25	254.4 /-140		B @ 3in FF		B @ 1st-2nd TR	B @3in FF				
16	2.63/-2.25	249.6/-138.4			B @1st-2nd TR			B @1st-2nd TR	B @1st-2nd TR		
17	3.5/-3	280.3/-157.6				B @FF-1st TR		B @FF-1st TR			
18	3.5	328.9			B @3rd-4th TR	B @3rd-4th TR		B @3rd-4th TR	B @3rd-4th TR		
	−3	−154.4	B @1st-2nd TR								
19	3.5	260									
	−3	−148.8									
20	5.25	282.2			B @2nd-3rd TR				B @2nd-3rd TR		
	−4.5	−160.8		1.5in. FR		4in. FR				B @1st-2nd TR	
21	5.25	234		B @ 11in FF			B @11in FF				
	−4.5	−146.3		4in. FR		5in. FR	1in. FR	1in. FR			
22	5.25	216									
	−4.5	−132.1		6in. FR		6in. FR	2.5in. FR	3in. FR			
23	7	214.9					B @17in FF				
	−6	−122.8		6.125in. FR	6in. FR	8in. FR	4.5in. FR	5in. FR	2in. FR WFR @1r1c & 1r2c		B @1st-2nd TR
24	7	187.4									0.75in. FR
	−6	−88.71			34% FR	34% FR		28% FR	28% FR		
25	8.75	185.8									
	−7.5	−73.27			42% FR	42% FR, WFR @1r1c, @1r2c		58% FR	58% FR		
26	8.75	156.7									1.5in. FR
	−7.5	−52.5			60% FR	60% FR		64% FR	64% FR		
27	10.5	153.6								1in. FR	
	−9	−47.48			73% FR	73% FR		75% FR	75% FR		
28	10.5	125.6								2.5in. FR	8in. FR
	−9	−37.12									
29	10.5	108.8	36.75in. FR							4in. FR	
	−9	−31.97			81% FR	81% FR		77% FR	77% FR		
30	10.5	98.35									
	−9	−28.22			81% FR	81% FR		77% FR	77% FR		

Note: The steel plate faces are abbreviated as follows: FE = the East Flange, NWW = West of North Web, NWN = North of North Web, NWS = South of North Web, SWW = West of South Web, SWN = North of South Web, SWS = South of South Web, NWE = East of North Web, and SWE = East of South Web. Also, FF means "from footing", FR is fracture, B is buckling, TR is tie row, WFR is tie weld fracture, r is tie row, and c is tie column

Table 2
Experiment log of Specimen C2 (Note: 1 in. = 25.4 mm; 1ft = 0.3048 m; 1sq in. = 645.2 mm^2; 1 in^4 = 416231 mm^4; 1 psi = 0.0069 MPa; 1 ksi = 6.9 MPa).

Cycle No	Cycle Drift, in	Laterally Applied Force, V, kips	FE	NWW	NWN	NWS	SWW	SWN	SWS	NWE	SWE
14	2.63/-2.25	301.3/-143.3		B @2in FF			B @2in FF				
15	2.63/-2.25	292.1/-141.7			B @3rd-4th TR	B @3rd-4th TR		B @3rd-4th TR	B @1st-2nd TR		
16	2.63/-2.25	285.4/-139.5				B @1st-2nd TR		B @2nd-3rd TR			
17	3.5/-3	319.8/-156.6	B @1st-2nd TR		B @1st-2nd TR	B @5th-6th TR					
18	3.5	303						B @3rd-4th TR			
	−3	−149.8									
19	3.5	294.1									
	−3	−143.9									
20	5.25	308.1									
	−4.5	−154.9		0.5in. FR			3.5in. FR	4.5in. FR			
21	5.25	259.9		B @13in FF							
	−4.5	−138.6		5.125in. FR		4in. FR	4.75in. FR	5.25in. FR			B @1st-2nd TR
22	5.25	240.4									
	−4.5	−125.3		6in. FR		5in. FR	5.25in. FR	6.5in. FR		B @1st-2nd TR	
23	7	230.9					B @13in FF				
	−6	−111.7		7.25in. FR	2.5in. FR	8in. FR WFR @1r1c	8.375in. FR	10.5in. FR WFR @1r2c	7.25in. FR		
24	7	198.7									
	−6	−80.98			42% FR	42% FR		46.4% FR	46.4% FR		
25	8.75	192.3			B @2nd-3rd TR	B @2nd-3rd TR			B @2nd-3rd TR		
	−7.5	−74.78			46% FR	46% FR		57.3% FR	57.3% FR, WFR @1r2c		
26	8.75	162.9									
	−7.5	−51.96			62.5% FR, WFR @1r1c, 1r2c, 1r3c	62.5% FR		54% FR	54% FR		
27	10.5	167									
	−9	−48.12			68.8% FR	68.8% FR		60.4% FR, WFR @1r3c	60.4% FR WFR @1r1c, 1r3c		
28	10.5	144.7							1.5in. FR		2.5in. FR
	−9	−39.41			70.8% FR, Tie F @2r2c	70.8% FR, WFR @2r1c, Tie F @2r2c		64.6% FR	64.6% FR		
29	10.5	126.6							2.75in. FR		3in. FR
	−9	–32.97			71% FR, WFR @2r3c	71% FR		66.7% FR	66.7% FR		
30	10.5	115.7							3in. FR		3.125in. FR
	−9	−28.53			73% FR	73% FR		68.75% FR	68.75% FR		

Note: The steel plate faces are abbreviated as follows: FE = the East Flange, NWW = West of North Web, NWN = North of North Web, NWS = South of North Web, SWW = West of South Web, SWN = North of South Web, SWS = South of South Web, NWE = East of North Web, and SWE = East of South Web. Also, FF means "from footing", FR is fracture, B is buckling, TR is tie row, WFR is tie weld fracture, r is tie row, and c is tie column

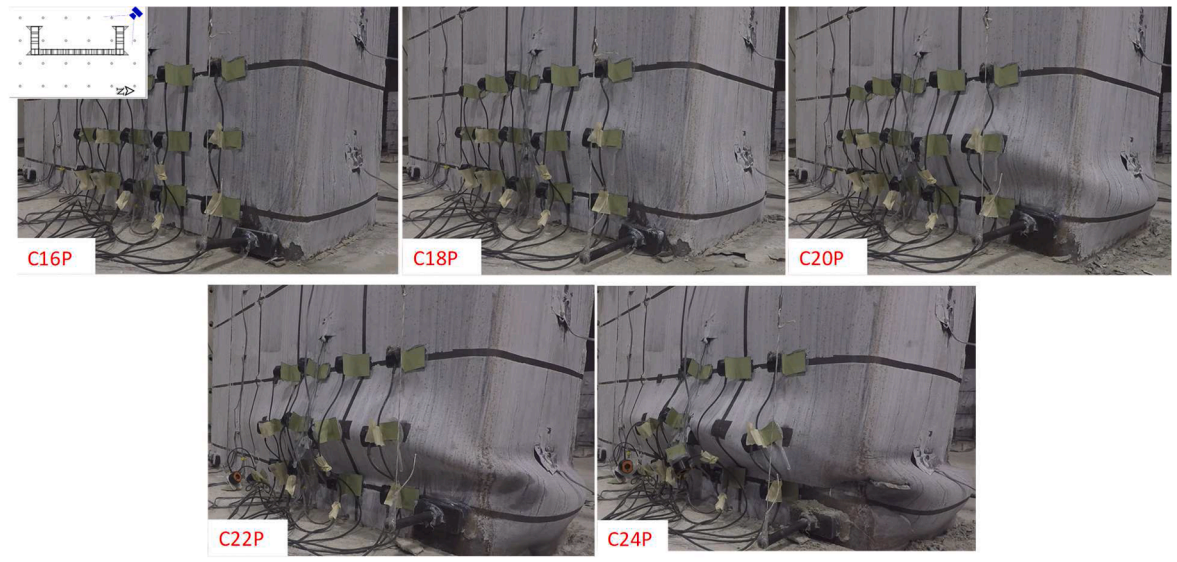

(a)

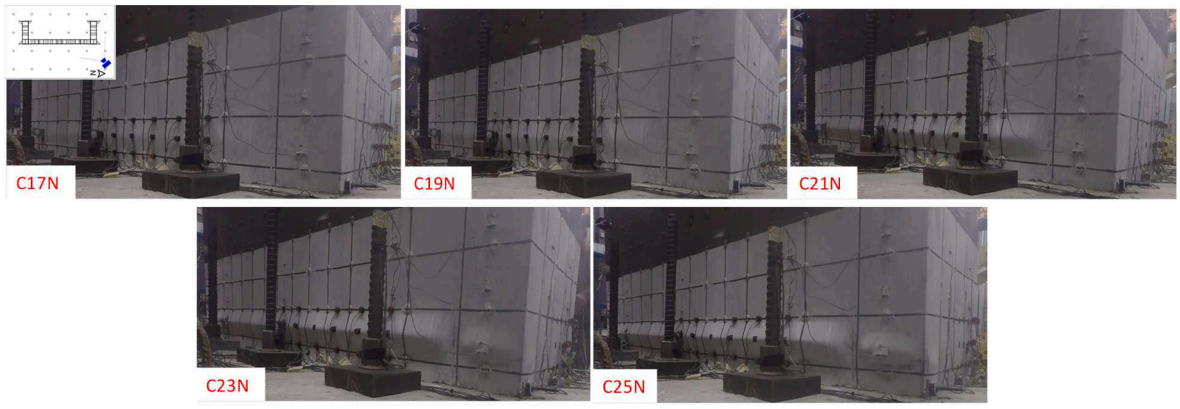

(b)

Fig. 10. Development of local buckling at lower part of Specimen C2 at different peak displacements at (a) the North Face of North Web (NWN), and; (b) The East face of Flange (FE).

6. Test results and observations

Both tests started by loading the vertical actuators while the horizontal actuators were held at zero displacement. The forces in the vertical actuators were increased up to their full capacity for Specimen C1 but up to the load closer to the target of 15% of $A_c f'_c$ on the cross-section of Specimen C2. The vertical actuators used to apply the axial load on the specimen were two MTS 243.90 T actuators with a nominal capacity of 450kips (2002kN) in tension. However, it turned-out that the controller only allowed the actuators to be loaded up to 425kips (1891kN), which resulted in application of 19% of $A_c f'_c$ on the cross section of Specimen C2, slightly short of the 22% initial target (note that the actuators are regularly calibrated, so the inability to apply the full 450kips (2002kN) could not be resolved). For Specimen C2, a force of 400kips (1779kN) was applied by each actuator in the early cycles, but it was subsequently dropped to 360kips (1601kN) to apply an axial force closer to the target of 15% of $A_c f'_c$ on the cross-section of the wall. This is because, in the early part of the test, the concrete strength was assumed to be 6ksi (41.4 MPa) but it was found out to be only 5.1ksi (35.2 MPa) from the cylinder tests (result became available after seven elastic cycle).

Then, the lateral actuators were loaded by applying lateral cyclic displacements at the top of the specimen according to the predetermined cyclic protocol. Both specimens were subjected to the same protocol. The first cycle of the loading protocol; at the displacement of $\Delta_y/4$; enabled to verify that all the attached data recording instruments were working properly and that no un-foreseen deficiencies existed in the specimen and the test setup. None of the components of steel plates of the specimen experienced any buckling or yielding and the same behavior was observed in all cycles at amplitudes of $\Delta y/2$, and 3 $\Delta y/4$. At the positive peak of the estimated displacement of Δy, no local buckling was observed.

At the lateral displacement equal to $2\Delta_y$' (i.e., Cycle 17), the lateral load capacity of Specimen C1 reached the maximum values of 280kips/-158kips (1245.5kN/-702.8kN) in the positive and negative drift directions, respectively. After the first cycle at the same drift, the test was stopped overnight and resumed the next day. In the process, the specimen was axially unloaded and reloaded following the same process of keeping actuators locked at zero displacement. When testing resumed, a peak maximum force of 328.9kips (1463kN) was reached in the positive direction of Cycle 18 (+3.5in. (89 mm)); this was apparently a glitch in the data acquisition process and this peak value is not considered a credible physical value when interpreting data later on. Likewise, the maximum lateral force of Specimen C2 was reached at the same lateral displacement equal to $2\Delta_y$' (i.e., Cycle 17), which were 319.8kips (1422.5kN)/ 156.6kips (-696.6kN) in the positive and negative drift

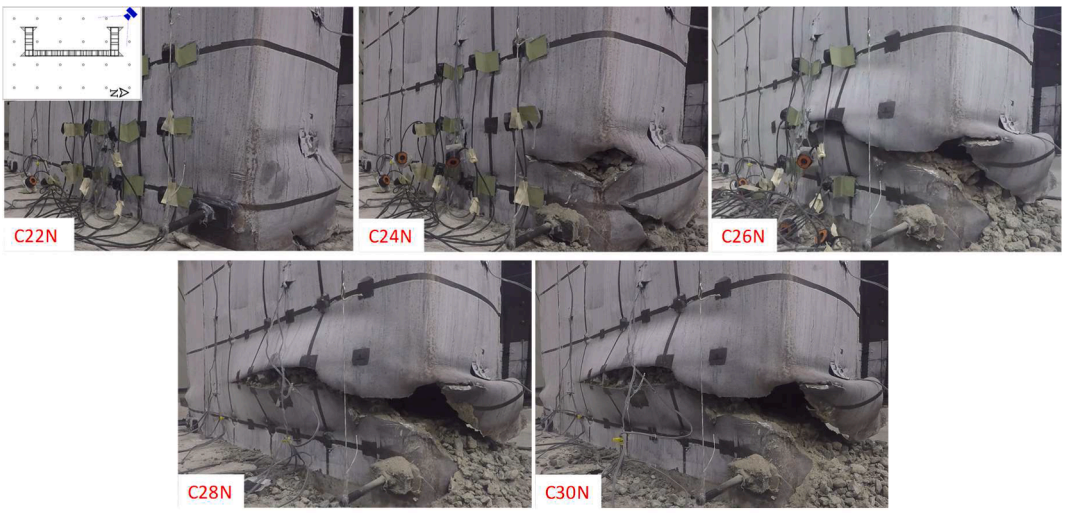

(a)

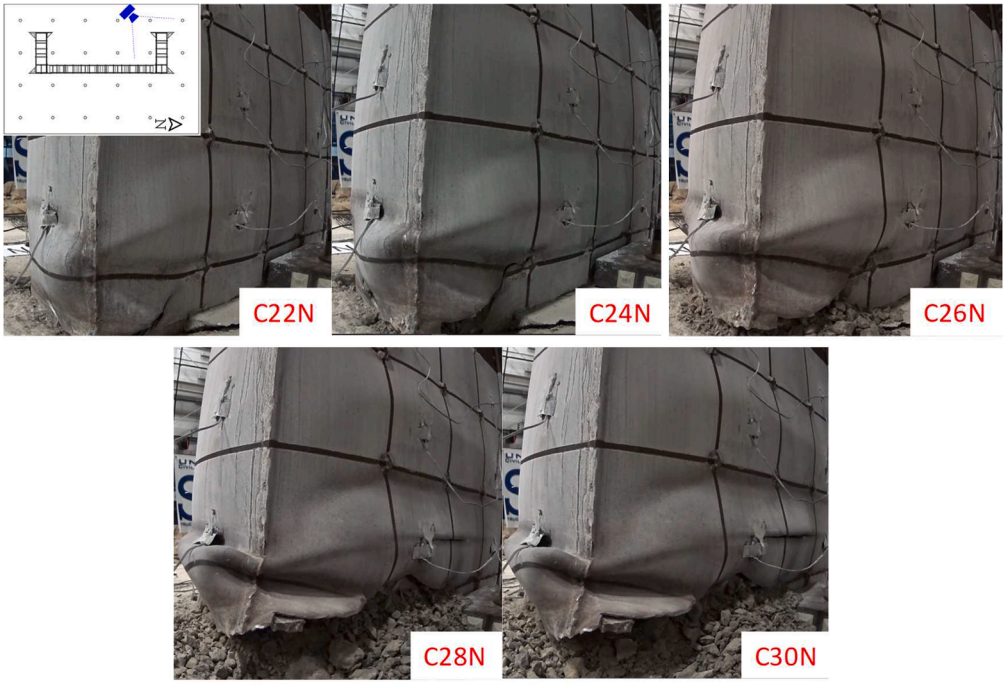

(b)

Fig. 11. Development of fracture at lower part of Specimen C2 at different peak displacements at (a) the North face of North Web (NWN), and; (b) the South Face of North Web (NWS).

directions, respectively.

6.1. Buckling

The strain gauge profiles were linear until the estimated yield displacement of Δ_y. At the positive peak of the estimated yield displacement of Δ_y, the strains recorded at the farthest end of the web and flange were −1941 and 779 μstrain, which correspond to 101.6 and 40.8% of the average measured yield strain (i.e., 1910μstrain) of the steel plate based on the coupon tests, for Specimen C1. The strains recorded at the same displacement for Specimen C2 were −2041 and 690μstrain, corresponding to 105 and 35% of the average measured yield strain (i.e., 1944μstrain based on coupons for Specimen C2). In the second excursion at the same drift, the strain values did not change much. No local buckling was observed at this cycle amplitude.

For Specimen C1, buckling was first visually observed during the second excursion of $1.5\Delta_y$' (+2.63in. (67 mm)/-2.25in. (57 mm)) displacement (i.e., Cycle 15), when local buckling was observed on the web at approximately 3in. (76.2 mm) from the top of the footing at the West face of the North Web (NWW), at the West face of South Web (referred to labeled as SWW afterwards) and between the 1st and 2nd tie rows on the South face of the North Web (referred to labeled as NWS afterwards). At peak displacement during the third excursion (i.e., Cycle 16), the steel plate between the 1st and 2nd tie rows also started to buckle at the North face of the South Web (referred to as SWN afterwards) and at the North face of the North Web (referred to as NWN afterwards), and at the South face of the South Web (referred to as SWS afterwards). Noticeable buckling also initiated at the East face of the Flange (referred to as FE afterwards) between the 1st and 2nd tie rows in the second cycle (i.e., Cycle 18) of the lateral displacement equal to $2\Delta_y$'

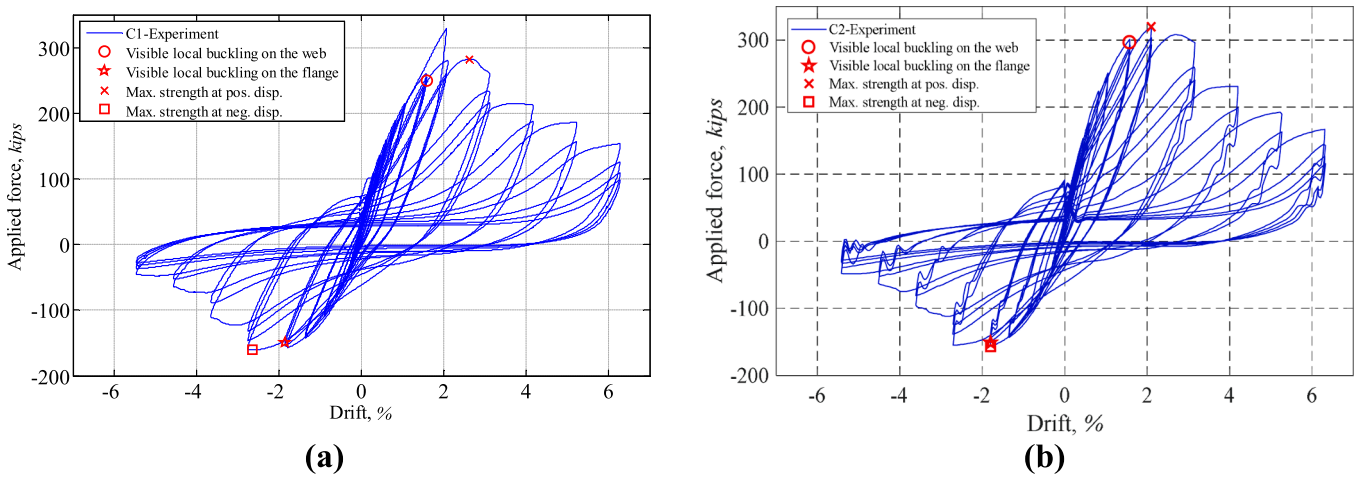

Fig. 12. Applied lateral force vs. top drift relationship for: (a) Specimen C1, and; (b) Specimen C2.

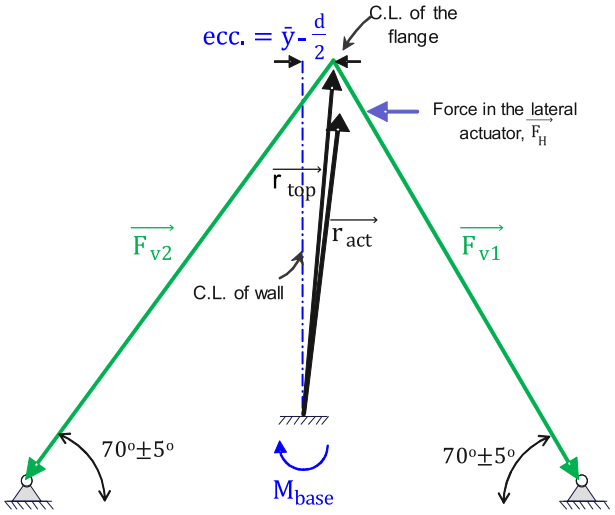

Fig. 13. Free-body diagram of the specimen wall at zero displacement.

(i.e., +3.5in. (89 mm)/-3.0in. (76 mm)). Other buckling that developed at other locations along the height of the specimen during the test are reported in Table 1 (and in [20]).

For Specimen C2, at the displacement amplitude of $1.5\Delta_y$' (i.e., Cycle 14), local buckling initiation was observed 2in. (50.8 mm) above the footing on NWW and on SWW, which is one cycle earlier than what was observed in Specimen C1. During the second excursion at the same drift (i.e., Cycle 15), local buckling was observed in the steel plate between the 1st and 2nd tie rows SWS and at peak displacement during the third excursion (i.e., Cycle 16), the steel plate between the 1st and 2nd tie rows started to buckle on NWS. At the lateral displacement equal to $2\Delta_y$' (i.e., Cycle 17), buckling was also observed to develop in the steel plate between the 1st and 2nd tie rows on NWN. In the negative drift direction, buckling started to initiate in the East face of Flange (FE) between the 1st and 2nd tie rows. In the second excursion at the same drift (i.e., Cycle 18), additional buckling was observed between the 1st and 2nd tie rows on SWN. Again, other locations where buckling was observed to develop as testing progressed are reported in Table 2 (and in [20]). Note that in Specimen C2, plates between the 2rd and 3rd tie rows buckled before it happened between the 1st and 2nd tie rows on NWS, NWN and SWN. However, the buckling waves of the steel plates between the 1st and 2nd tie rows ended up to be larger by the end of the test than at any other locations.

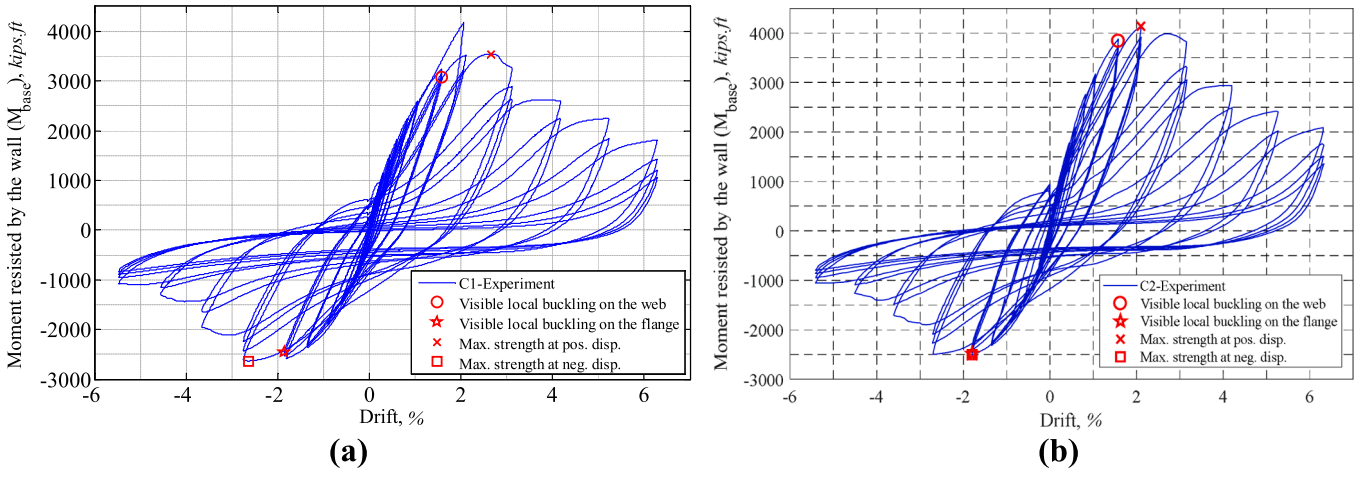

Fig. 14. Calculated experimental base moment vs. top drift relationship for: (a) Specimen C1, and; (b) Specimen C2.

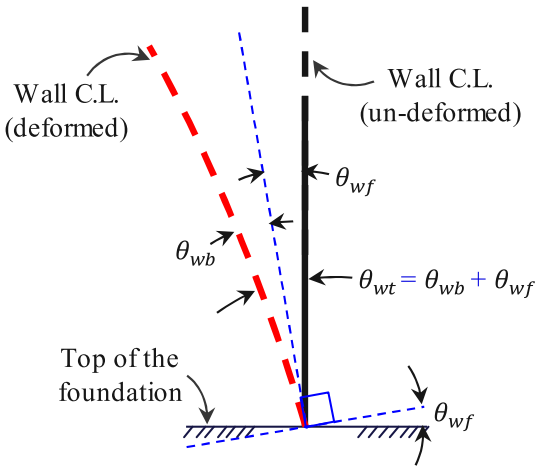

Fig. 15. Composition of wall rotations at the base of the wall.

6.2. Fracture

In Specimen C1, in the negative drift of the first cycle (i.e., Cycle 20) of $3\Delta_y$' displacement (i.e., +5.25in. (133 mm)/-4.5in. (114 mm)), a fracture started to occur at the corners of NWS and NWW at the footing level and propagated towards the buckled locations on each side, following an inclined path, approximately 4in. (102 mm) long at NWS and 1.5in. (38 mm) at NWW. In the second excursion (i.e., Cycle 21), the cracks on NWS and on NWW grew and another fracture was observed to initiate at the corner of SWW and SWN at 1in. (25.4 mm) above the top of the footing, being approximately 1in. (25.4 mm) in length on both sides. Cracks continued to grow in subsequent cycles (refer to Table 1 (and in [20]) for more details). In the second excursion (i.e., Cycle 24) of the $4\Delta_y$' displacement (i.e., +7in. (178 mm)/-6in. (152 mm)), where the drop in lateral horizontal force in the positive direction was 34.7% and 23.7% in the negative direction, closure plates of both the North and South webs completely fractured. At that point, 34% of the web length (8.25in. (209.6 mm) out of 24in. (609.6 mm)) on the North Web (referred to as NW this point forward) and 28% of web length (6.75in. (171.5 mm) out of 24in. (609.6 mm)) on the South Web (referred to as SW this point forward) was fractured. Fracture percentages progressively grew and at the end of test, 81% of the web length on NW and 77% of web length on SW was fractured. Also, a 36.75in. (933.5 mm) long fracture was measured at the footing level on FE in the third cycle (i.e., Cycle 29) of the $6\Delta_y$' displacement amplitude (i.e., +10.5in. (267 mm)/-9in. (229 mm)). There were fractures in the welds of some tie bars. Other details of fracture propagation are provided in Table 1 (and in [20]).

For Specimen C2, similar behavior was observed. Fracture also started in the first cycle (i.e., Cycle 20) of $3\Delta_y$' displacement (i.e., +5.25in. (133 mm)/-4.5in. (114 mm)), except that this time, the lateral horizontal force at that point dropped by about only 4% and 10% in the positive and negative drift direction, respectively. The steel fractured at the corners of NWS and NWW; and SWN and SWW at the footing level, over a length of 0.5in. (12.7 mm) on NWW, 3.5in. (88.9 mm) on SWW and 4.5in. (114.3 mm) on SWN. Cracks continued to grow in subsequent cycles (refer to Table 2 (and in [20]) for details). During the second excursion (i.e., Cycle 24) of the $4\Delta_y$' displacement (i.e., +7in. (178 mm)/-6in. (152 mm)), the drop in lateral horizontal force in the positive and negative drift direction became 27.9% and 28.8%, respectively, closure plates of both North and South webs completely fractured, and 42% of the web length at NW and 46.4% of web length at SWW were fractured. Fractures percentages progressively grew and at the end of test, 73% of the web length at NW and 69% of web length at SW was fractured. There was no fracture on the FE of this specimen. However, a tie bar fractured at the 2nd horizontal and 2nd vertical row of ties (where vertical lines are numbered starting from the tip of the web, i.e. farthest point from the flange).

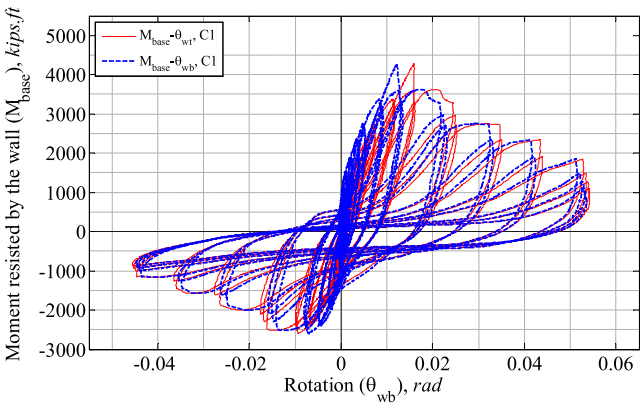

Fig. 16. Comparison of calculated experimental base moment vs. wall base rotation and vs. total base rotation for Specimen C1.

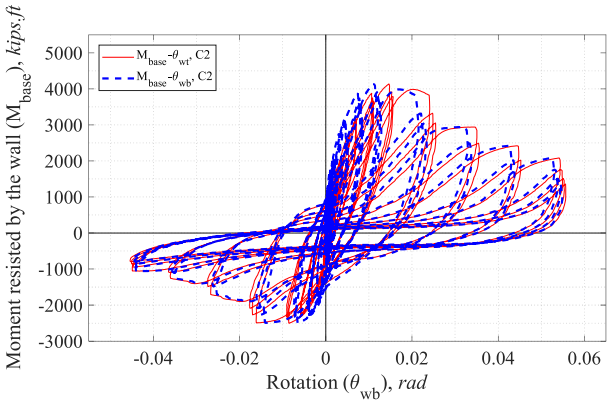

Fig. 17. Comparison of calculated experimental base moment vs. wall base rotation and vs. total base rotation for Specimen C2.

To illustrate the parts of the above behavior, Fig. 10 shows local buckling at the lower part of the Specimen C2 for different peak displacements. Fig. 11 shows fracture in Specimen C2. Both Figures are representative of the behavior of both specimens. Labels *CnP* and *CnN* in these figures refer to peak positive and negative displacements during Cycle n. For example, *C16P* means the maximum positive displacement attained during the sixteenth cycle during the test.

7. Comparison of results

The experimentally obtained applied lateral force versus top lateral drifts for Specimens C1 and C2 are shown in Fig. 12a and 12b, respectively. The vertical axis shows the horizontal force applied to the specimen, which is equal to the value recorded by the lateral actuators (not equal to the shear force applied to the specimen, because the force shown in this figure is not yet corrected to subtract the horizontal components of the vertical actuator forces, which only cancel each other when the drift is equal to zero). The lateral drift was calculated by dividing the top of the wall's lateral displacement by the distance from top of the footing to the centerline of the lateral actuator's attachment head. The points when some of the key observations were made during the test (corresponding to the onset of visible local buckling on the web and flange and maximum strengths at negative and positive displacements) are marked on these curves.

As mentioned earlier, the recorded peak of 328.9kips (1463kN) shown in Fig. 12a is an outlier believed to be due to a recording error in the data acquisition system, and this value was not taken into account in the subsequent calculations when referring to wall strength. Such a

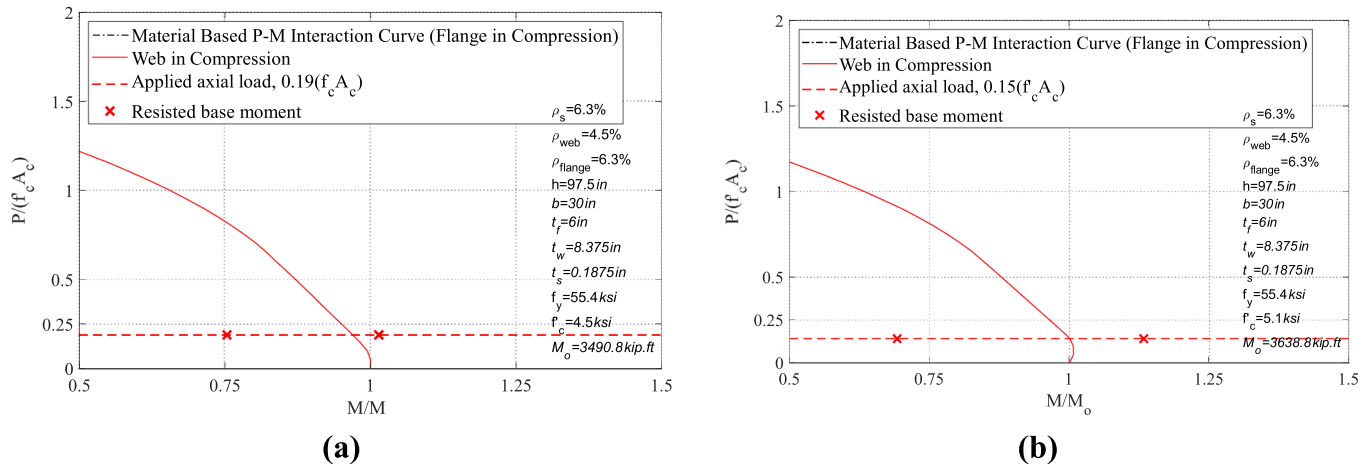

Fig. 18. Comparison of: (a) Specimen C1, and; (b) Specimen C2 flexural resistances with P-M interaction curve (where$M_0 = M_p$).

Table 3
Actual, nominal, and expected material properties and calculated flexural resistances for Specimens C1 and C2 (Note: 1 in. = 25.4 mm; 1ft = 0.3048 m; 1sq in. = 645.2 mm^2; 1 in^4 = 416231 mm^4; 1 psi = 0.0069 MPa; 1 ksi = 6.9 MPa).

Specimen	Material property	Concrete f'_c, *ksi*	Steel plates F_y, *ksi*	M_y, *kip.ft*				M_{PSDM}, *kip.ft*				$\frac{M_{PSDM}}{M_y}$		$\frac{M_{exp}}{M_{PSDM}}$	
				Pos.	y_{NA}, in	Neg.	y_{NA}, in	Pos.	y_{NA}, in	Neg.	y_{NA}, in	Pos.	Neg.	Pos.	Neg.
C1	Nominal	4.0	50.0	2079	7.52	−1507	9.52	3010	6.19	−2406	4.86	1.45	1.6	1.18	1.10
	Actual	4.5	55.4	2356	8.35	−1634	8.92	3387	6.27	−2640	4.64	1.44	1.62	1.04	1.00
	Expected	5.1	55.0	2486	8.78	−1632	8.60	3596	6.40	−2662	4.19	1.45	1.63	0.98	1.0
C2	Nominal	4.0	50.0	2100	8.15	−1449	9.05	3044	6.25	−2359	4.60	1.45	1.63	1.35	1.06
	Actual	5.1	55.4	2516	9.52	−1581	8.53	3639	6.92	−2623	4.00	1.45	1.66	1.13	0.96
	Expected	5.1	55.0	2506	9.51	−1573	8.53	3624	6.96	−2608	3.99	1.45	1.66	1.14	0.97

Note: y_{NA} is the location of the neutral axis from the face of flange.

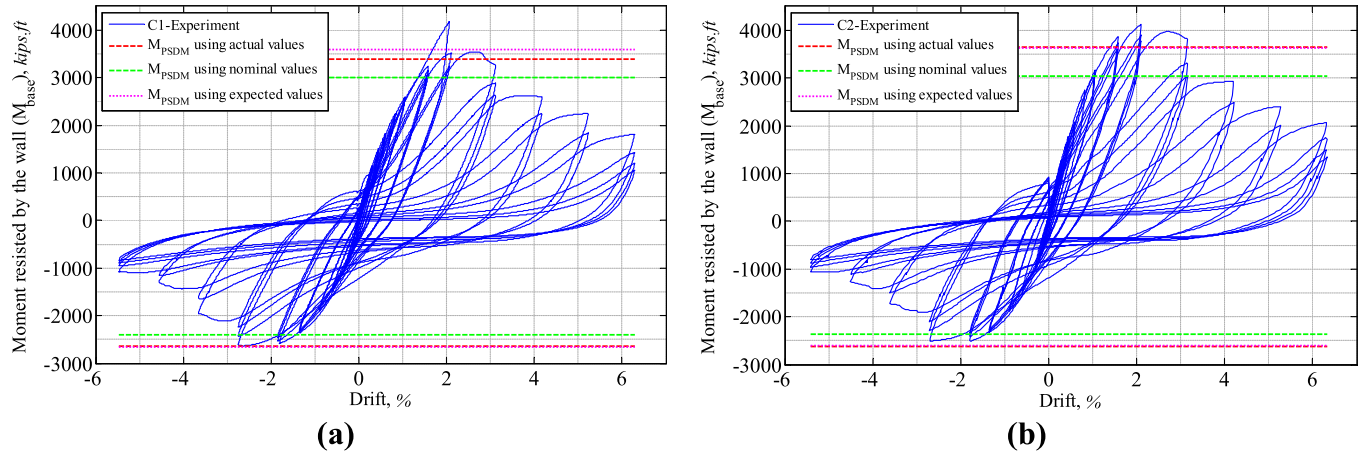

Fig. 19. Comparison of calculated theoretical resistance moments and the experimental base moment for: (a) Specimen C1, and; (b) Specimen C2.

spurious peak was not observed in the test result of Specimen C2.

The moment resisted by the wall at its base was calculated according to the free-body diagram shown in Fig. 13 and by Eq. (1) in order to correct for the eccentricity of the vertical load about the centroid of the wall cross–section, and for the resultant horizontal force from the vertically inclined actuators that the horizontal actuators resisted as the wall drifted during test:

$$\overrightarrow{M_{base}} = \overrightarrow{r_{act}} \times \overrightarrow{F_H} + \overrightarrow{r_{top}} \times \left(\overrightarrow{F_{v1}} + \overrightarrow{F_{v2}}\right) \quad (1)$$

where $\overrightarrow{M_{base}}$ is the moment resisted at the base, $\overrightarrow{r_{act}}$ is the location vector of the horizontal actuator, $\overrightarrow{F_H}$ is the force in the horizontal actuators, $\overrightarrow{r_{top}}$ is the location vector of the top of the wall (at the centroid of flange), and $\overrightarrow{F_{v1}}$ and $\overrightarrow{F_{v2}}$ are the force vectors of the East and West vertically inclined actuator, respectively.

Fig. 14a and 14b show the calculated base moment resisted by the wall versus the top of the wall's drift for Specimen C1 and Specimen C2, respectively.

To determine the ductility (μ), an effective yield displacement ($\delta_{y,eff}$) was taken as the displacement corresponding to the intersection of a line tangent to the initial slope of the resulting pushover curve and a horizontal line set at the level of the maximum base moment obtained from

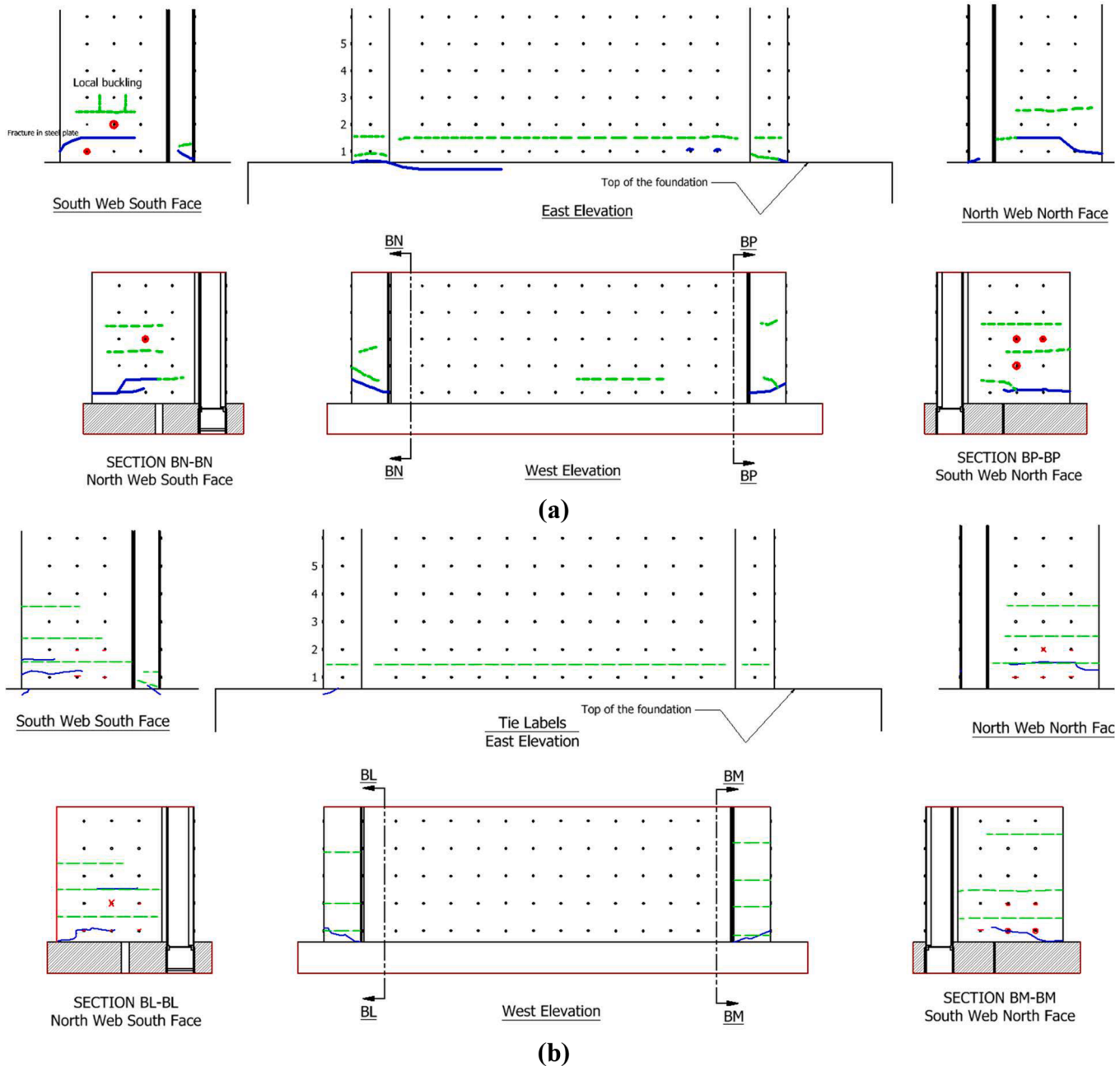

Fig. 20. Post-test damage inspection of the wall steel plates for: (a) Specimen C1, and; (b) Specimen C.

test, $M_{base,\max}$. The displacement obtained at $0.8M_{base,\max}$ after post-peak of the backbone curve of the test setup was taken for the ultimate displacement (δ_u). Then, using Eq. (2), ductility was calculated and was found to exceed 4 (i.e., 4.02/-4.3 for positive and negative directions for both specimens).

$$\mu = \frac{\delta_u}{\delta_{y.eff}} \tag{2}$$

The rotations of the wall at the base where the plastic hinge was developed was also calculated. This was done using the recorded horizontal movements of the wall for the string pot attached to the wall closest to the footing, and then dividing its readings by its distance to the top of the footing (i.e., 33in.), which resulted in total rotations at the wall base (i.e., θ_{wt}). Recognizing that this calculated rotation also included the rotations of the wall-footing connection (i.e., θ_{wf}), these rotations at the wall-footing connection (θ_{wf}) were subtracted from the total rotations (θ_{wt}) to obtain the wall rotations at the base (i.e., θ_{wb}). Fig. 15 shows the composition of the rotations at the base of the wall. Note that there was no slippage between the footing and the strong floor during the test and therefore the lateral displacements of the footing were considered zero in calculation of the rotation.

Note that the rotation at the wall-footing connection (θ_{wf}) could have been calculated at each step of the test using the differences in the recorded displacements from the vertical string pots (i.e., along the axial axis of the wall) that were connected from the wall surface to the footing's top surface at east and west elevations of the wall, divided by their distance from each other, but this would have not included rotations introduced locally near the base of the wall due to the flexibility/deformations of the footing itself. Instead, the wall-footing connection rotation was taken into account by substituting the footing and wall-to-footing connection with a linear rotational spring at the base of the wall. The rotational stiffness of this spring was calculated by finding the slope

of a line that was fitted to the M_{base}-θ_{wf} relationship curve at the linear cycles (i.e., from the beginning of the test until end of Cycle 7) and then multiplying the rotational stiffness by the base moment (M_{base}) at each corresponding step of the test. The rotational spring stiffness was calculated as 1.13×10^6kip-ft./rad (1.53×10^9kN-mm/rad) for Specimen C1 and 1.26×10^6kip-ft./rad (1.71×10^9kN-mm/rad) for Specimen C2. Figs. 16 and 17 show the calculated base moment versus the wall rotations (M_{base}-θ_{wb}) relationship curve as well as comparison to the ones with total rotations at the wall base (M_{base}-θ_{wt}) for Specimens C1 and C2, respectively.

The points of maximum flexural strength experimentally obtained from Specimens C1 and C2 were compared to their corresponding values predicted by theoretical P-M interaction curves. These plots are shown in Fig. 18a and 18b for Specimens C1 and C2, respectively. In calculation of the P-M interaction curves, the actual material properties of the steel plates and concrete infill measured from the tensile coupon and compression cylinder tests were used. The interaction curves were obtained by fiber section analyses using OpenSees [26].

Table 3 summarizes the actual, nominal, and expected material properties and calculated flexural resistances (accounting for the applied axial load) for Specimens C1 and C2. The actual strengths are calculated using values obtained from the testing of steel coupons of samples from the wall's web and flanges, and of concrete cylinders cast during construction of the walls and tested on the corresponding specimen test day. The nominal strengths are calculated using the specified yield values for the steel plates, namely 50ksi (345 MPa) for the A572Gr50 steel, and for the concrete ordered as a 4ksi (27.6 MPa) concrete from the supplier. The expected strengths are calculated using the specified steel yield and concrete compressive strengths multiplied by $R_y = 1.1$ and $R_c = 1.5 \times 0.85$, respectively.

The experimentally obtained moments developing at the base of the walls were also compared to their theoretical strength calculated using the Plastic Stress Distribution Method (PSDM). The theoretical values were calculated using the actual, nominal, and expected material properties, as described above. Comparisons are shown in Fig. 19a and 19b for Specimens C1 and C2, respectively. Values of the yield moment, M_y (when ε_y first reached in cross-section) are also included in Table 3. These were calculated for strain diagrams obtained assuming an E_c values using ACI Eq. [27] (note that lower values of with E_c would give lower M_y values).

Fig. 20a and 20b shows a schematic of the damage on the steel plates for Specimens C1 and C2, respectively, at completion of the tests. In this figure, the locally buckled areas are marked with dashed lines, the fracture lines are shown with solid line, the failed tie welds are shown with dots and failed tie bar in Specimen C2 are shown by crosses. Note that failures at tie locations, in all observed cases, were due to weld failure at their connection (typically at only one end of the tie) except for one tie bar in Specimen C2 (identified by the red cross in Fig. 20b where the tie itself is known to have fractured). The failed end of the tie is marked in the figure.

8. Summary and conclusions

Two large-scale C-shaped Composite Plate Shear Wall/Concrete Filled were subjected to axial and cyclic flexural loading. The walls were subjected to 19% and 15% axial loading before horizontal cyclic loads were applied. Both specimens showed similar buckling and fracture behaviors. Ductility was more than 4 (4.02/-4.3 for positive and negative directions for both specimens) when flexural strength dropped to 80% of the peak value developed, and both specimens reached or exceeded their calculated plastic moment capacities in the positive and negative direction. More specifically:

- Peak strength was reached at drifts of 3.2% in the positive and 2.7% in the negative directions for Specimen C1. On the other hand, the peak strength was observed at 2.1% and 1.8% in the positive and negative directions for Specimen C2.
- Tests showed that even though local buckling started in early cycles after yielding, the capacity of the walls did not drop until fracture of the steel plates.
- The fractures of steel plate were not sudden; it was progressive, meaning that flexural strength degradation was relatively slow.
- A significant portion of web and flange remained unfractured at peak drifts of 6.3/-5.4% when testing was stopped, and a residual flexural strength of 29.7/-31.3% and 32.9/-31.8% of corresponding peak values of Specimens C1 and C2 in the positive and negative directions, respectively, remained after completion of the tests.
- Yielding propagated over roughly 40% of the height of the wall; given that the ratio of Plastic Moment to First Yield Moment was in the range of 1.45 to 1.66 (depending on direction of loading) for the measured material strengths.
- Buckling occurred between multiple layers of tie bars, as a consequence of yielding over a substantial part of the height.
- Even though the main purpose of the tests was to observe the behavior of the walls under different axial loading, they ended up to be relatively close to each other. However, as it is generally considered essential to achieve replicability of results across multiple specimens, the availability of test results on two specimens that have achieved essentially similar hysteretic behavior is positive to ensure the reliable seismic performance of the system.

Based on the experimental observations and results obtained, it can be concluded that C-shaped C-SPW/CF can exhibit good cyclic behavior without premature strength degradation, while maintaining their ability to resist large axial load of up to 19% $A_c f'_c$.

Credit authorship contribution statement

Hadi Kenarangi: Software, Validation, Formal analysis, Investigation, Writing - review & editing, Visualization, Data curation, Conceptualization. **Emre Kizilarslan:** Software, Validation, Investigation, Formal analysis, Data curation, Writing - review & editing, Visualization. **Michel Bruneau:** Supervision, Project administration, Writing - review & editing, Visualization, Conceptualization, Methodology, Funding acquisition.

Declaration of Competing Interest

The authors declare that they have no known competing financial interests or personal relationships that could have appeared to influence the work reported in this paper.

Acknowledgments

This research was conducted with support from the Charles Pankow Footing (CPF) and the American Institute of Steel Construction (AISC), through CPF research grant #06-16 awarded to co-PIs Amit Varma, from Purdue University, and Michel Bruneau, University at Buffalo. The brief project description presented above focuses on the part of the work conducted at the University at Buffalo only. The researchers also thank Magnusson Klemencic Associates (MKA), Cives Steel Co., J.F.Stearns Co., and Turner Construction, for donating steel and fabrication of specimens tested. The researchers are also grateful to members of the Project Advisory Team for their technical guidance.

References

[1] MSC, 850-FT-TALL rainier square tower tops out in only 10 months. Modern Steel Construction, 2019. Retrieved from: https://www.aisc.org/modernsteel/news/2019/august/rainier-square-tower-tops-out-at-850-ft-in-under-10-months/.
[2] Bowerman, H. and J.C. Chapman, Bi-steel steel-concrete-steel sandwich construction, in: Composite construction in steel and concrete IV. 200p. 656-667.

[3] Varma, A.H., et al. Steel-plate composite (SC) walls for safety related nuclear facilities: design for in-plane and out-of-plane demands. In: Proceedings of the 21st IASMiRT Conference (SMiRT 21). 2011.
[4] Varma AH, et al. Steel-plate composite (SC) walls for safety related nuclear facilities: Design for in-plane forces and out-of-plane moments. Nucl Eng Des 2014; 269:240–9.
[5] Bhardwaj SR, Varma AH. Design of modular steel-plate composite walls for safety-related nuclear facilities. American Institute of Steel Construction; 2017.
[6] Varma AH, et al. Seismic behavior and modeling of high-strength composite concrete-filled steel tube (CFT) beam–columns. J Constr Steel Res 2002;58(5–8): 725–58.
[7] Varma AH, et al. Seismic behavior and design of high-strength square concrete-filled steel tube beam columns. J Struct Eng 2004;130(2):169–79.
[8] Stephens MT, Lehman DE, Roeder CW. Seismic performance modeling of concrete-filled steel tube bridges: Tools and case study. Eng Struct 2018;165:88–105.
[9] Kenarangi H, Bruneau M. Experimental Study on Composite Action in Reinforced Concrete-Filled Steel-Tube Shaft Foundations. J Bridge Eng 2019;24(7):04019060.
[10] Denavit MD, Hajjar JF, Leon RT. Cross-Section Strength of Circular Concrete-Filled Steel Tube Beam-Columns. Engineering Journal-American Institute of Steel Construction 2016;53(2):99–105.
[11] Hajjar JF. Concrete-filled steel tube columns under earthquake loads. Prog Struct Mat Eng 2000;2(1):72–81.
[12] Leon RT, Kim DK, Hajjar JF. Limit state response of composite columns and beam-columns part 1: Formulation of design provisions for the 2005 AISC specification. Engineering Journal-American Institute Of Steel Construction 2007;44(4):341.
[13] Brown N, Kowalsky M, Nau J. Impact of D/t on seismic behavior of reinforced concrete filled steel tubes. J Constr Steel Res 2015;107:111–23.
[14] Tsai, K.-C. Design of steel beam-to-box column connections for seismic load'. In: Proc., First Worm Conf. Constructional Steel Design, Acapulco, Mexico. 1992.
[15] Usami T, Ge H. Ductility of concrete-filled steel box columns under cyclic loading. J Struct Eng 1994;120(7):2021–40.
[16] Alzeni, Y. and M. Bruneau, Cyclic Inelastic Behavior Of Concrete Filled Sandwich Panel Walls Subjected To In-Plane Flexure. Technical Rep. MCEER 14-009, 2014. MCEER The State University of New York at Buffalo.
[17] Yu J-G, et al. Experimental Study of Composite Steel Plate Shear Wall with Flush End-Plate Connection. International Journal of Steel Structures 2019:1–20.
[18] Eom T-S, et al. Behavior of double skin composite wall subjected to in-plane cyclic loading. J Struct Eng 2009;135(10):1239–49.
[19] Cho SG, et al. Seismic capacity estimation of Steel Plate Concrete (SC) shear wall specimens by nonlinear static analyses. KSCE J Civ Eng 2015;19(3):698–709.
[20] Bruneau, M. and E. Kizilarslan, Seismic and Wind Behavior and Design of Coupled CF-CPSW Core Walls for Steel Buildings. Interim Report No.5 to Charles Pankow Foundation: Grant # 06-15, 2019.
[21] DSI, DYWIDAG-SYSTEMS INTERNATIONAL. 2019. Retrieved from https://www.dsiamerica.com/.
[22] Lehman DE, Roeder CW. Foundation connections for circular concrete-filled tubes. J Constr Steel Res 2012;78:212–25.
[23] Bruneau, M., H. Kenarangi, and E. Polat, Seismic and Wind Behavior and Design of Coupled CF-CPSW Core Walls for Steel Buildings. Interim Report No.1 to Charles Pankow Foundation: Grant # 06-15, 2017.
[24] Bruneau, M., H. Kenarangi, and T.P. Murphy, Contribution of Steel Casing to Single Shaft Foundation Structural Resistance. National Cooperative Highway Research Program, NCHRP Research Report 872, Transportation Research Board; National Academies of Sciences, Engineering, and Medicine, Washington, D.C., 2018: p. 178 pages (plus 287 pages of Appendices available online at https://apps.trb.org/cmsfeed/TRBNetProjectDisplay.asp?ProjectID=3406).
[25] LSTC, LS-DYNA keyword user's manual Version R7.0. Vol. 970. 2013, Livermore Software Technology Corporation (LSTC), California.
[26] McKenna, F., S. Mazzoni, and G. Fenves, Open System for Earthquake Engineering Simulation (OpenSees) Software Version 2.2. 5. University of California, Berkeley, CA. Available from http://opensees.berkeley.edu, 2016.
[27] ACI. Building code requirements for structural concrete (ACI 318–19) and commentary. American Concrete Institute; 2019.